The roles of planetary and gravity waves during a major stratospheric sudden warming as characterized in WACCM

Varavut Limpasuvan [a,*], Jadwiga H. Richter [b], Yvan J. Orsolini [c], Frode Stordal [d], Ole-Kristian Kvissel [d]

[a] Department of Chemistry and Applied Physics, Coastal Carolina University, Conway, SC, USA
[b] National Center for Atmospheric Research (NCAR), Boulder, CO, USA
[c] Norwegian Institute for Air Research (NILU), Kjeller, Norway
[d] Department of Geosciences, University of Oslo, Oslo, Norway

ARTICLE INFO

ABSTRACT

The roles of planetary waves (PWs) and gravity waves (GWs) are examined during a realistic major stratospheric sudden warming (SSW), simulated in the National Center for Atmospheric Research Whole Atmosphere Community Climate Model (WACCM). This major SSW event is characterized by a well-separated polar stratopause during a wind-reversal period. Formed by adiabatic warming induced by westward GW drag, the early-winter stratopause layer appears at its climatological level. With the incipient wind reversal and SSW onset, this layer plunges ~20 km in time, as the amplified PW interacts with the mean flow. The SSW recovery starts in the upper mesosphere as GW drag becomes eastward due to the filtering effects of the underlying wind. During this recovery, the stratopause reforms at an elevated altitude due to adiabatic warming induced by strong upper mesospheric PW forcing. Intensified downward motion from the mesosphere then ensues as the stratopause descends toward its climatological position.

© 2011 Elsevier Ltd. All rights reserved.

1. Introduction

A "stratospheric sudden warming" (SSW) event greatly alters the Northern Hemisphere (NH) wintertime polar atmosphere (Andrews et al., 1987). The polar vortex can undergo strong displacement off the pole or splits into two smaller vortices (e.g. Manney et al., 2008; 2009). In a zonally averaged sense, the climatologically strong polar eastward wind can greatly weaken (minor SSW) or becomes westward ("major" SSW) while the polar stratospheric temperature rapidly warms by several degrees.

Despite its name, the meteorological influence of a major SSW permeates beyond the stratosphere. Ground-based lidars and space-borne infrared observations indicate polar mesospheric cooling (as much as 20 K) during SSW onset (Siskind et al., 2005; Thayer and Livingston, 2008). Likewise, the anomalous westward wind during a major SSW can readily propagate down toward the tropopause as planetary waves (PWs) interact with the background flow (Baldwin and Dunkerton, 1999, 2001). Near the tropopause, the wind anomaly can induce strong momentum forcing by the synoptic-scale waves to drive a mean circulation that extends the (anomalous) westward wind toward the surface (Limpasuvan et al., 2004).

Changes in the lower mesosphere and upper stratospheric region during a major SSW can strongly impact stratospheric chemistry. Persistent wind reversal during SSW coincides with an episode of stratopause "separation" (Hitchman et al., 1989). Related to the lower mesospheric cooling, this separation commences as the stratopause (formed initially near its climatological position) descends ~10–20 km toward the middle stratosphere with SSW onset (von Zahn et al., 1998; Manney et al., 2009). In NASA Microwave Limb Sounder measurements (Manney et al., 2008a, 2009) or in simulations by the National Center for Atmospheric Research (NCAR) Whole Atmosphere Community Climate Model (WACCM) (Kvissel et al., under review), descent of mesospheric air, rich in carbon monoxide (CO), is observed to occur in association with this stratopause plunge, penetrating as far down as 30 km. As the vortex recovers, the stratopause reforms much higher in altitude normally associated with the mesosphere (e.g., near 72–75 km) as shown in Manney et al. (2008b) and Orsolini et al. (2011). This reformed stratopause drops back toward its climatological level as polar vortex re-strengthens, along with enhanced polar descent of mesospheric minor species into the stratosphere (Lee et al., 2011). In particular, observations show an *enhanced* amount of dry mesospheric air (rich in NO_x) descending well below 60 km, as the vortex recovers from SSW (e.g. Randall et al., 2009; Orsolini et al., 2010).

Traditionally, the strong polar variability during SSWs is linked to PWs and their interactions with the circumpolar flow (Matsuno, 1971; Andrews et al., 1987). During SSWs, PW amplitude can greatly

* Corresponding author. Tel.: +1 843 349 2826.
E-mail address: var@coastal.edu (V. Limpasuvan).

amplify and PW momentum and heat flux convergence can strongly decelerate the polar night jet, inducing a strong (residual) descent motion over the pole that contributes to the adiabatic warming of the stratospheric polar region. However, the smaller scale gravity waves (GWs) can also play a role in SSWs (Siskind et al., 2005). Based on early GCM generation that includes the middle atmosphere, Pawson (1997) suggested that GWs can trigger strong wintertime polar vortex disturbances like SSW. Richter et al. (2010) reported that GWs can alter how PWs propagate into the stratosphere and subsequently influence the occurrence frequency of SSWs. Furthermore, Ren et al. (2008) noted that the observed wind reversal (from eastward to westward) during a major SSW can selectively allow eastward propagating GWs to impose an eastward drag in the mesosphere that leads to polar mesospheric cooling, as suggested by Holton (1983) and Liu and Roble (2002). To date, while the roles of GW are recognized as crucial in maintaining the middle atmospheric structure (Andrews et al., 1987; Fritts and Alexander, 2003), their forcings and their evolution during SSWs are not well understood (Limpasuvan et al., in review; Yamashita et al., 2010).

Recent advances in global climate models (GCMs) with high altitude extension and increasingly high spatial resolution (e.g. Sato et al., 1999; Watanabe et al., 2008) can provide first order clues into how PWs and GWs interplay during major SSWs. The NCAR's WACCM version 3.5 (WACCM3.5) can simulate the atmosphere (with parameterized GW effects) up to about 145 km and has generated very realistic NH wintertime climatology (Garcia et al., in preparation). While most current GCMs tend to exhibit slight cold bias in the winter vortex that diminishes SSW frequency, this WACCM3.5 wintertime climatology has SSW occurrence frequency that is comparable to the observed rate of about 6 SSWs per decade (Charlton et al., 2007; Richter et al., 2010). As such, the recent WACCM runs serve as *useful tools* to improve our understanding of SSW.

To this end, the present paper examines the relative roles of PWs and GWs in forcing the circulation changes through the course of a major SSW event, as simulated in WACCM3.5. To our knowledge, an explicit interplay between PWs and GWs in producing a realistic major SSW and in promoting the enhanced polar descent from the mesosphere has not been documented. The results below reveal that a major SSW event reflects an interrupted period of climatological polar descent driven by westward GW drag that leads to the stratopause separation. We note the important roles of stratospheric PWs in the descent of the stratopause formed early in the winter, and the roles of mesospheric PWs as the newly reformed stratopause (at an elevated altitude) falls back to its climatological position. We also show the changing GW effects during SSWs in connection with the vortex recovery as the wind alternates. Without the occurrence of SSW, the stratopause maintains its climatological level throughout the winter with sustained westward GW forcing.

2. Model and methodology

Based on the NCAR Community Atmospheric Model, version 3.5, WACCM3.5 has a horizontal (latitude × longitude) resolution of $1.9° × 2.5°$ (latitude × longitude) and a variable vertical resolution, with 66 vertical levels. In all, the model domain extends up to ~145 km, capturing the entire mesosphere. While PWs and synoptic-scale waves are resolved, the influence of the much smaller scale GWs are accounted for through parameterizations. Stationary orographic GWs are parameterized based on the scheme of McFarlane (1987). The non-orographic GW propagation parameterization is based on the scheme of Lindzen (1981) and wave sources are assumed to be generated by convection or synoptic storms. Based on the source parameterization of Beres et al. (2005), the convectively generated GW source spectrum is activated at the top of deep

convection as defined by Zhang and McFarlane (1995). As discussed in Richter et al. (2010), the synoptic storm source is based on the regions of strong wind deformation and temperature gradient as identified by the frontogenesis function of Hoskins (1982) at 600 hPa.

In replacing the arbitrarily (and traditionally) specified GW source spectrum parameterization with multiple schemes that accounts for various possible sources (frontal genesis, convection, and orography) linked to model-generated tropospheric quantities, WACCM3.5 is able to significantly improve the resulting NH stratospheric variability in the simulations (Garcia et al., in preparation). More importantly, WACCM3.5 also includes an additional parameterization to estimate mountain stress due to the unresolved orography (given the model's coarse resolution). This added mountain stress has large effects on the frequency of SSWs in the model climatology by altering the propagation of PWs into the wintertime polar vortex (Richter et al., 2010). Previous simulations with WACCM (like most GCMs) tended to generate an anomalous cold polar middle atmosphere in which the SSW occurrence was sparse (Charlton et al., 2007). The inclusion of a new turbulent mountain stress formulation allowed for the parameterized gravity waves to breaking at higher levels and kept the simulated middle atmosphere from being too cold. In fact, with its current state of GW parameterization (despite the oversimplification of non-orographic GW sources) and the mountain stress, the SSW occurrence frequency simulated in WACCM3.5 is remarkably similar to that of observations.

Parameterized GW effects are generally considered poorly constrained by observations (Fritts and Alexander, 2003). However, the reasonably parameterized GWD in WACCM, as outlined here, are expected to have fairly generic effects in responding to the modeled dynamics and to be similar to the effects that occur in nature. Based on the improved realism of the model's climatology, details of how the parameterized GW actually dissipates are of less importance as shown by McLandress and Scinocca (2005). However, the magnitude and detailed vertical structure of the GW effects would be dependent on the model set-up.

Currently, a 55-year run of WACCM3.5 has been made starting at 1955. The basic climatology and statistics of SSW in this run are presented by Garcia et al. (in preparation). This run includes solar and anthropogenic forcings and incorporates observed sea surface temperatures (SST). Because the model does not resolve GWs, the quasi-biennial oscillation (QBO) is incorporated into the model by relaxing the tropical winds (on a 10-day timescale) to the observed QBO winds between 86 and 4 hPa and between 22°N and 22°S. As described in Garcia et al. (2007), the run has interactive chemistry with realistic boundary conditions and includes observed solar cycle variability and anthropogenic forcings. The run is part of a four-member ensemble set made for the Chemistry-Climate Model Validation Activity, version 2 (CCMVAL2) (Richter et al., 2010).

Based on the World Meteorological Organization (WMO) definition of a major SSW (wintertime wind reversal at 10 hPa), 33 major SSWs are identified in the 55-year WACCM run. From these SSWs, 12 events exhibit westward wind anomaly descent of more than 10 days to the tropopause that is followed by westward polar wind near the surface. Among these 12 events, the NH winter of 1979–1980 are selected for this case study since this winter has a relatively quite solar activity. As such, this particular SSW event allows for the examination of the representative dynamics, stratopause separation and mesospheric air descent as presented here and in the accompanying paper (Kvissel et al., under review). A detailed branch run is then conducted using the October 1979 output of the 55-year archived run as the initial condition. This branch run is performed till May 1980 and the results are output every 3 hours with key dynamical variables, diagnostics for the parameterized GW forcings, and important chemical species to examine the mesospheric descent. For this chosen event, the QBO is in its eastward phase.

The *Transform Eulerian Mean* (TEM) diagnostic framework is used to examine the zonal-mean dynamics in the simulation. From Andrews et al. (1987; p. 128), the wave forcing and zonal-mean wind tendencies can be related by the equation:

$$\left(\frac{\partial \overline{u}}{\partial t}\right)_{TEM} = \left\{\frac{1}{\rho_o a \cos\varphi}\nabla\cdot\overrightarrow{F} + \overline{X}\right\} + \left\{-\overline{v}^*\left[\frac{1}{a\cos\varphi}\frac{\partial}{\partial\varphi}(\overline{u}\cos\varphi) - f\right] - \overline{w}^*\frac{\partial\overline{u}}{\partial z}\right\}$$

(1)

The zonal–mean zonal wind tendency is influenced by the *total wave forcing* (the first set of braces) and the *advection term* due to the residual circulation (the second set of braces) given as starred quantities. The total wave forcing consists of the divergence of the Eliassen-Palm (EP) flux ($\overrightarrow{F}$) of the resolved waves and the drag imposed by the parameterized GWs ($\overline{X}$).

3. NH polar evolution

Fig. 1 illustrates the simulated 1979–1980 major SSW through the altitude-time evolution of the zonal–mean zonal wind and temperature over the polar region (averaged between 60°N–80°N). In the late fall and early winter (prior to December 19), pulses of eastward wind dominate the polar region below 80 km, and westward wind (gray region with blue contours) appears predominantly above 80 km. Around December 19, the wind below (above) 80 km begins to switch to westward (eastward) direction. The stratosphere around 40–50 km undergoes a warming of nearly 10 K as the core of the warm stratopause layer (solid line in temperature contour) descends from its climatological position (around 60 km) to about 45 km by December 31. The polar wind throughout the stratosphere is dominated by the westward flow before returning to the eastward direction around January 12. Thereafter, the warm stratopause reforms at an elevated position (near 70 km) before descending toward its climatological position, as the eastward flow penetrates down to the near-surface level. Overall, the simulated evolution of the wind and temperature bears a strong resemblance to major SSW observations (Manney et al., 2008; 2009; Orsolini et al., 2010) as noted in the Introduction.

The meridional and vertical components of the residual circulation ($\overline{v}^*$ and $\overline{w}^*$) are shown on Fig. 1c and d, respectively. Strong
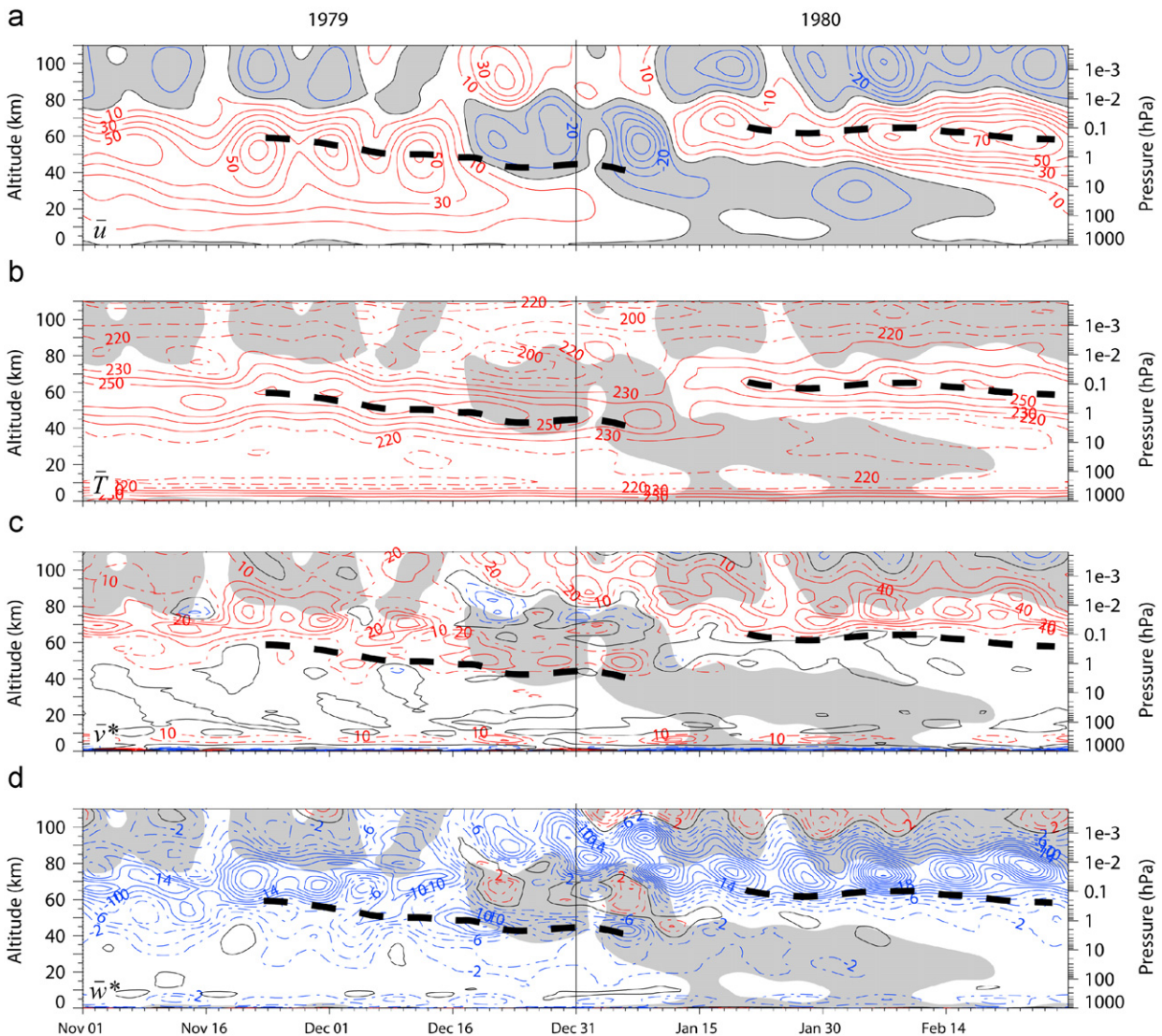

Fig. 1. Time–altitude evolution of the zonal–mean zonal wind (m/s) (a), temperature (deg K) (b), and the meridional component (m/s) (c) and vertical component (mm/s) (d) of the residual circulation averaged between 60°N–80°N. Positive (negative) contours are given red (blue) with zero-value contour in black. Except for temperature, dashed colored lines have smaller contour interval than solid lines. Temperature greater than (less than) 230 K is shown as solid (dashed) lines. Thick black line marks the approximate central location of the warm stratopause layer. Gray regions indicate westward zonal-mean zonal wind.

poleward and downward motion (solid contours) persists between 60 and 80 km prior to the wind reversal around December 19. Between December 19 and January 9, this downward (and poleward) pattern tends to descend with the zero-wind line on bottom edge of the gray region, in coincidence with the falling warm stratopause layer (Fig. 1b). Above this descending warm layer, we see a weak rising (equatorward) motion along the upper region of the westward wind in association with the anomalously cold mesospheric air (less than 200 K). Furthermore, above the gray westward wind region, we note a persistently strong downward and equatorward pattern between 80 and 100 km, along with the changes below. After January 9, the circulation tends to return to the pattern noted before December 16 but is relatively stronger above 60 km.

The zonal–mean zonal wind tendency in the simulation (Fig. 2a) is largely accounted for by the wind tendency according to TEM (Fig. 2b; LHS of Eq. (1)) as patterns of alternating wind acceleration tend to agree. Between 25 and 55 km, the wind tendency correlates well with the total wave forcing pattern (Fig. 2c). For example, between November 16 and December 11, the alternating episodes of wind deceleration and acceleration (centered near 55 km) appear to align with the alternating bands of westward and eastward wave forcing. However, in the regions where the meridional circulation is largest (as noted in Fig. 1), the total wave forcing tends to differ markedly from the wind

tendency. In particular, over these regions, the wind tendency is relatively weaker (as suggested by the zero nodal line around 60–80 km in Fig. 2a and b), and the wave forcing manifests itself more through the induced circulation, as seen in the SSW studies of Hsu (1981) and Dunkerton et al. (1981). Hence, while the advection terms in Eq. (1) due to the induced residual circulation tends to offset the wave forcings, this offset is greatest where the meridional circulation is strongest (compare Fig. 2d and e with Fig. 2c).

The decomposition of the total wave forcing into those by the resolved waves and parameterized GWD is shown in Fig. 3. In comparing the combined PW forcing and GWD (Fig. 3a) with the total wave forcing (due to GWD and all resolved waves; Fig. 2c), we note that PW forcing makes the largest contributions to the resolved waves. The decomposition of Fig. 3a into contributions by PWs (Fig. 3b) and GWD (Fig. 3c and d) further reveals that the total wave forcing above 55 km is dominated by non-stationary GWD. The influence from the stationary GWD (i.e. orography GWD) is relatively weak and is focused mainly between 45 and 75 km. Over the polar region, the contributions of GWD from convections are very little compared to those GWD components shown here.

The frontogenesis GWD (generated by synoptic storms) constitutes nearly all of the non-stationary GWD and dominates the total wave forcing between 60 and 85 km (see Fig. 3a). In that
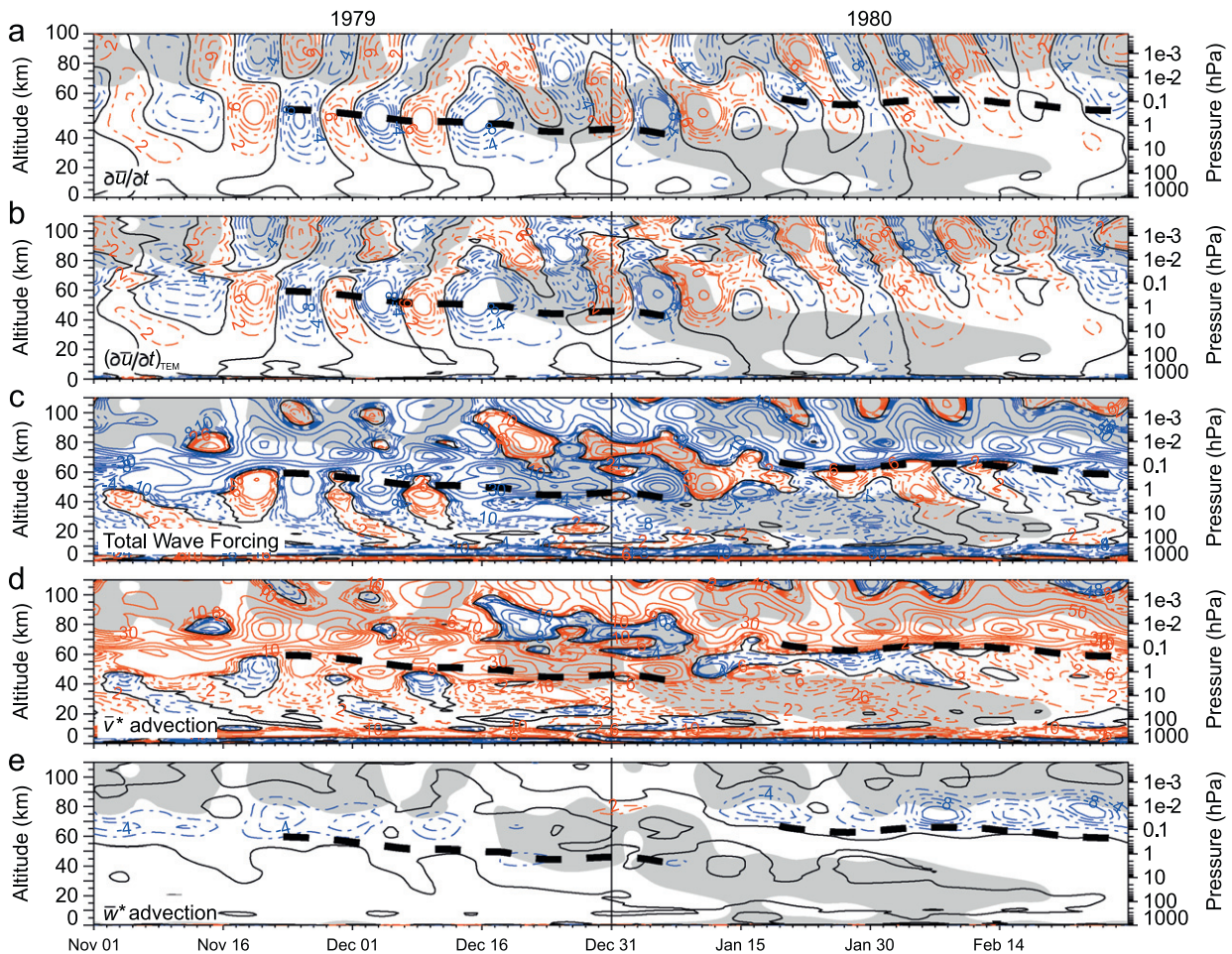

Fig. 2. Time–altitude evolution of the zonal–mean zonal wind tendency as simulated (a) and as determined by TEM (b) in Eq. (1). (c) The total wave forcing due to all resolved waves and GW drag as shown in the first brace on the RHS of Eq. (1). Advection terms by meridional ($\bar{v}^*$) and vertical ($\bar{w}^*$) residual circulation in the second brace on the RHS of Eq. (1)d–e. The sum of (c), (d), and (e) is equal to (b). All values are averaged between 60°N–80°N. Positive (negative) contours are given red (blue) with zero-value contour in black. Dashed lines have smaller contour interval than solid lines.
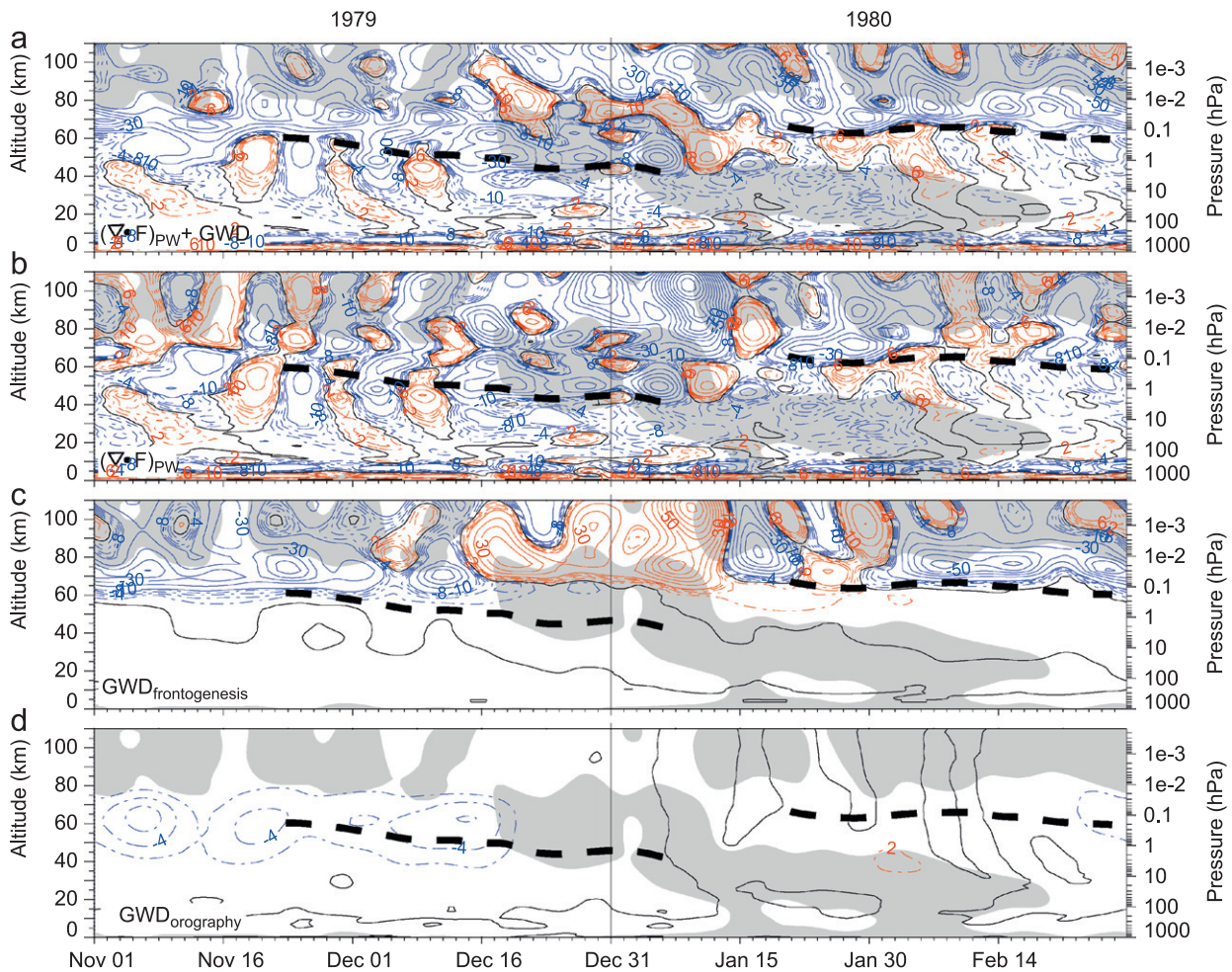
Fig. 3. Time–altitude evolution of the zonal-mean wave forcing by resolved planetary waves (PWs) and gravity wave drag (GWD) (a), by just resolved PWs (b), by nonstationary GWD due to frontogenesis (c), and by stationary GWD due to orography. All values are averaged between 60°N–80°N. Positive (negative) contours are given red (blue) with zero-value contour in black. Dashed color lines have smaller contour interval than solid lines. Thick black line marks the approximate central location of the warm stratopause layer.

vertical range and prior to the stratospheric wind reversal, the frontogenesis GWD consistently accelerates the wind westward to diminish the polar night jet strength, while the weaker PW forcing alternates between westward (blue contour) and eastward (red contour) acceleration. Reflected in the total wave forcing, this persistent westward GWD acceleration induced a strong poleward and downward residual circulation shown in Fig. 1c and d. Based on the TEM equation, this residual circulation tends to alleviate the strong, localized wave effects through the advection effects and Coriolis torque as shown in Fig. 2d and e. While the strong GWD is not reflected in the wind tendency, the induced downward motion would tend to maintain the warm stratopause (as noted in Fig. 2b) through adiabatic warming (Hitchman et al., 1989). The relatively smaller orographic GWD (Fig. 3d) contributes to the westward frontogenesis GWD and the resulting adiabatic warming (through downward motion) at a lower altitude range in the mesosphere.

Between 40 and 60 km, the PW forcing becomes amplified and persistently westward starting from December 10 (as the wind reverses direction) to early January (Fig. 3b). This occurrence parallels to a pattern of induced residual poleward and downward motion (see Fig. 1c and d and Fig. 2d and e) that tracks the lower portion of the westward wind (gray) region. The downward motion and the associated adiabatic warming coincide with the falling warm stratopause layer that drops to ~45 km by

December 31 (noted in Fig. 1). The directional change of the stratospheric wind filters out much of the orography GWD and its forcing becomes diminished between 40 and 60 km (Fig. 3d). The descent of the zero wind line (on the lower portion of the westward wind region) toward the lower stratosphere during a major SSW has been noted by observations as part of the PW-mean flow interactions (e.g. Liu and Roble, 2002; Limpasuvan et al., 2004). The suppression of orography GWD in the mesosphere by the stratospheric wind reversal below has been noted to correlate with the separated winter stratopause as it plunges downward from its climatological position (Hitchman et al., 1989; Siskind et al., 2005).

As the stratospheric wind becomes westward, the frontogenesis GWD above 60 km switches to eastward forcing as the westward propagation GWs are hindered by the westward stratospheric wind during SSW (Fig. 3c) (also noted by Holton (1983) and Liu and Roble (2002)). Between 70 and 80 km, this eastward GWD induces episodic upward and equatorward motion in the upper portion of the westward wind (gray region) as seen in Fig. 1c and d. The adiabatic cooling of the rising air appears to be responsible for the cold anomalies above the descending warm stratopause layer that straddles the lower part of the westward wind region (Fig. 1b). Such upward motion and the resulting cooling of the lower mesosphere during SSW were also noted by Liu and Roble (2002) and Ren et al. (2008). Above 80 km, while much of the non-stationary GWD effects are negated by the strong PW forcing, the initially strong eastward

GWD pulse around December 19 promotes the reversal of the upper mesospheric/lower thermospheric wind from westward to eastward direction as seen in the wind tendency (Fig. 2a and b).

The recovery of the polar atmosphere from the major SSW is marked by the return of westward wind in the upper mesosphere and the eastward wind in the lower mesosphere/upper stratosphere (LMUS) region. This return is punctuated by the re-appearance of the warm stratopause layer around its climatological position of 60 km (see Fig. 1a). The upper mesospheric wind recovery appears to occur soon after the wind reversal in the upper stratosphere. Around New Year, the eastward wind between 80 and 100 km has noticeably weakened in conjunction with the persistent westward PW forcing that dominates the total wave forcing (see Fig. 3a and b). From December 25 to January 12, this westward PW forcing appears to induce a very strong residual downward pattern that traces the zero wind line in the upper westward wind (gray) region. The associated adiabatic warming around 80 km potentially promotes the return of the warm stratopause layer at an elevated level. This strong PW westward forcing is due largely to the zonal wavenumber 1 distur-bance, as shown in Fig. 4. Siskind et al. (2005) noted strong PW amplitude in the upper mesosphere and remarked that the subse-quent wave dissipation would lead to similar poleward and down-ward motion (and polar warming) via downward control (Garcia and Boville, 1994).

The LMUS wind recovery appears to be associated with the wave driving of both PWs and GWs. In Fig. 3a, just after New Year, we see a band of eastward forcing (red contours) along the upper edge of the westward wind (gray region). This band eventually descends along with the zero wind to about 40 km around January 15. Prior to this band's descent, the eastward forcing is made up of the eastward GWD (Fig. 2c) between 60 and 70 km. As SSW recovery draws near 15 January, eastward PW forcing (predominantly from zonal wavenumber 1; Fig. 4) provides the most forcing. This combined eastward forcing induces a relatively weak equatorward and upward motion that descends with time with the westward (gray) region after New Year (see Fig. 1c and d).

Finally, as the polar wind and temperature recover from this major SSW, the persistent westward GWD resumes roughly between 60 and 85 km. This westward GWD drives a strong poleward and downward motion much like the pattern noted prior to SSW. This circulation helps maintain the warm stratopause layer which now re-appears near its climatological position.

As shown in Fig. 3c, frontogenesis GWD plays the largest contribution to the momentum budget compared to orography GWD. Prior to the major SSW onset, Fig. 5 shows that the westward GWD (blue contours) between 60 km and 80 km is derived from GWs of phase speed between $+/-15\,\mathrm{m\,s^{-1}}$
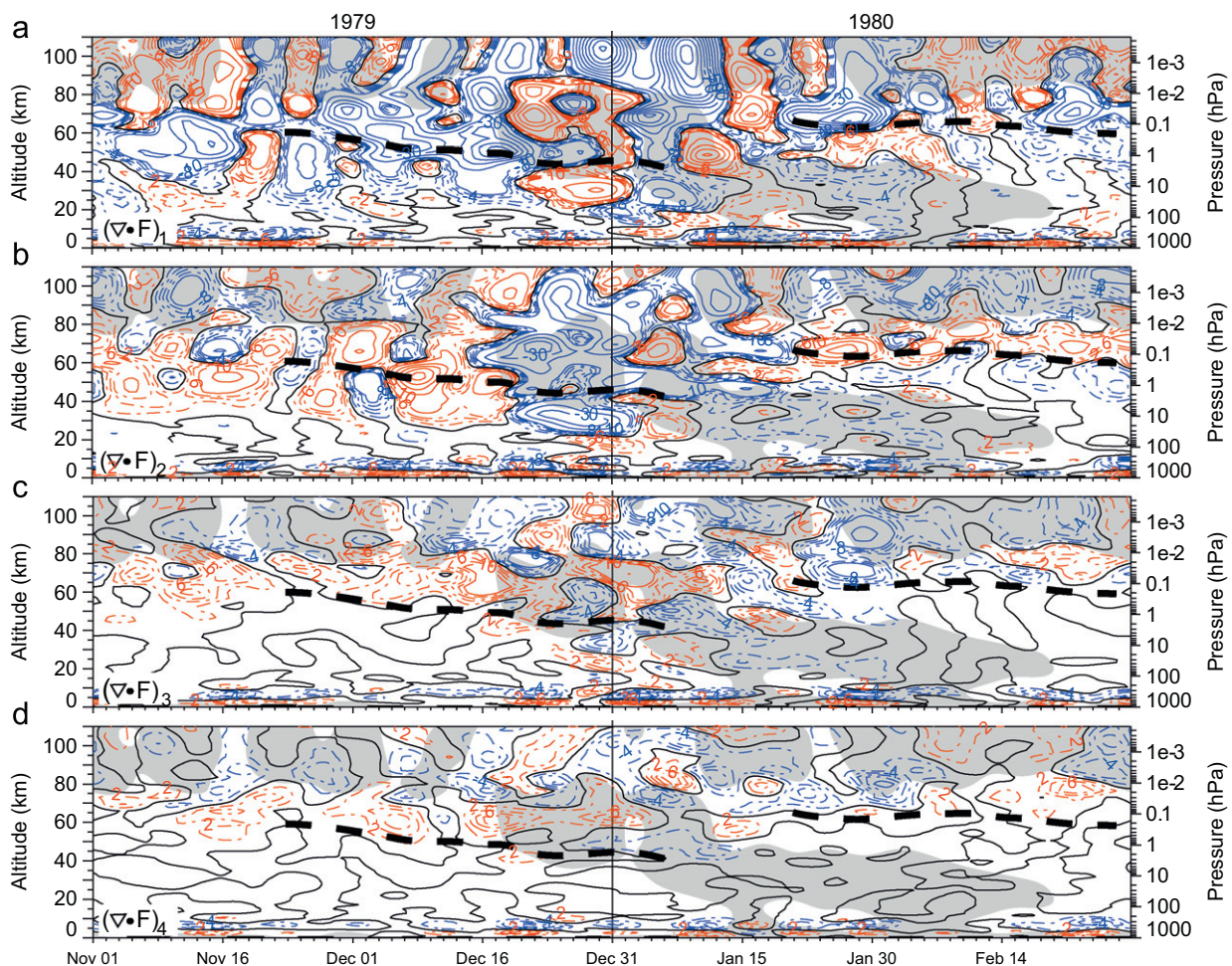

Fig. 4. Time–altitude evolution of the zonal-mean PW wave forcing due to its wavenumber 1–4 components (a–d). All values are averaged between 60°N–80°N. Positive (negative) contours are given red (blue) with zero-value contour in black. Dashed color lines have smaller contour interval than solid lines. Thick black line marks the approximate central location of the warm stratopause layer.
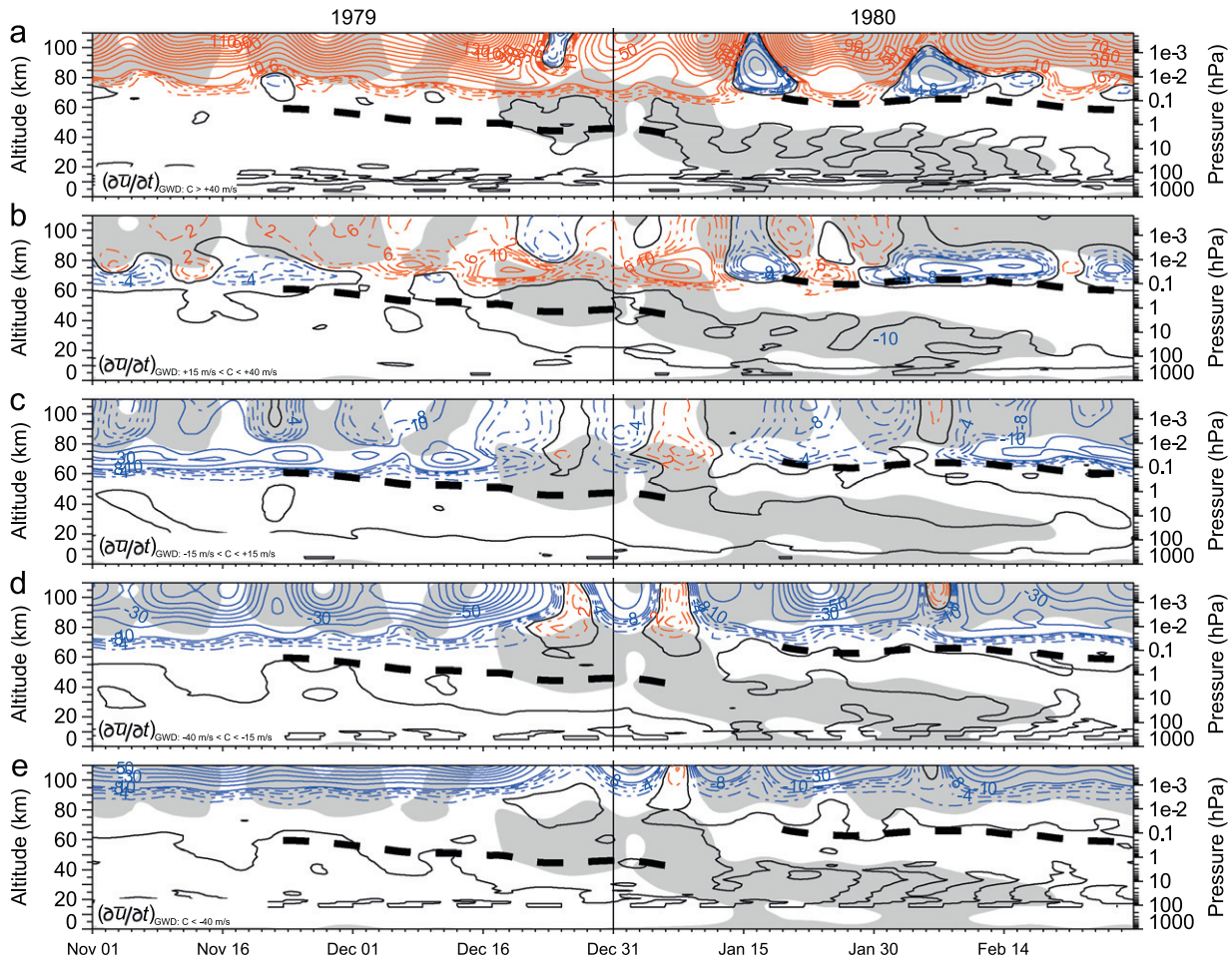
Fig. 5. Time–altitude evolution of the zonal-mean, non-stationary GWD as contributed by GWs of phase speed greater than +40 m/s (a), between +15 and +40 m/s (b), between –15 and +15 m/s (c), between –40 and –15 m/s (d), and less than –40 m/s (e). Here, positive (negative) speed indicates eastward (westward) wave. All values are averaged between 60°N–80°N. Positive (negative) contours are given red (blue) with zero-value contour in black. Dashed color lines have smaller contour interval than solid lines.

(Fig. 5c), with added contribution by other westward propagating GWs (Fig. 5d and e). Eastward propagating GWs of phase speed between 40 and 15 m s^{-1} contributes slightly to this westward forcing in November. After the SSW recovery, the westward GWD comprises mainly of eastward propagating GWs of phase speed greater than 15 m s^{-1} (Fig. 5a and b). Regardless, the net westward GWD prior to and after SSW induces the strong downward motion that maintains the warm stratopause layer at its climatological position. During SSW (between December 16 and January 16), eastward propagating GW (red contours) dominates the net GWD noted in Fig. 3c. In particular, between 60 and 80 km, eastward forcing from GWs of phase speed between 40 and 15 m s^{-1} impart the most influence to the total wave forcing noted in Fig. 3a.

In zonally averaging the zonal wind and GWD as presented in Fig. 5, pockets of unexpected wave drag may appear inconsistent with the background wind. For example, around, January 16 in Fig. 5a, we note the appearance of westward forcing by GWs of eastward phase speed in excess of 40 m s^{-1} in the region of westward wind (gray region) around 80–100 km. This inconsistency is due to the appearance of strong and localized eastward polar flow with wind speed in excess of 40 m s^{-1} (see also the last row and column plot of Fig. 6 below). In such localized region, the ground-relative eastward GWs can be westward relative to the flow and their damping can produce strong localized westward forcing. Hence, while the overall zonally averaged wind may be

westward and weak, the zonally averaged GWD by eastward GW can appear as westward forcing. During this time period, the vortex is also highly evolving in recovering from SSW.

Fig. 6 illustrates the NH polar stereographic maps of frontogenesis (orography) GWD at 77 (63) km where the peak amplitude is found in Fig. 3c and d. The corresponding geopotential height is also displayed as black contour lines. Prior to and after SSW (as represented by November and January 16), the predominance of westward frontogenesis GWD poleward of 60°N is consistent with Fig. 3c. Since frontogenesis GWD is based on the synoptic-scale disturbance and launched at 600 hPa in a column wise manner in WACCM, we also show the temperature distribution at 600 hPa (left column in Fig. 6) along with areas of strong wind speed (gray region). From this, we see that the frontogenesis GWD tends to collocate with areas of strong tropospheric flow curvature (like over the Arctic Ocean, south of Greenland, and Scandinavia on January 16) and temperature gradients (fronts). Prior to and after SSW, the vortex below (e.g. at 63 km) has a high degree of zonal symmetry with strong circumpolar flow (mainly eastward zonal-mean polar wind) that allows westward GWD (from the launched GW source spectra) to mainly impact the circulation at 77 km. During SSW (December 20 and 31), the frontogenesis GWD switches to eastward forcing in areas poleward of 60°N as noted in Fig. 3c. This change is due to filtering effects of the flow below where the vortex exhibits a wavenumber 2 signature (as reflected in the resolved wave forcing shown on Fig. 4b).
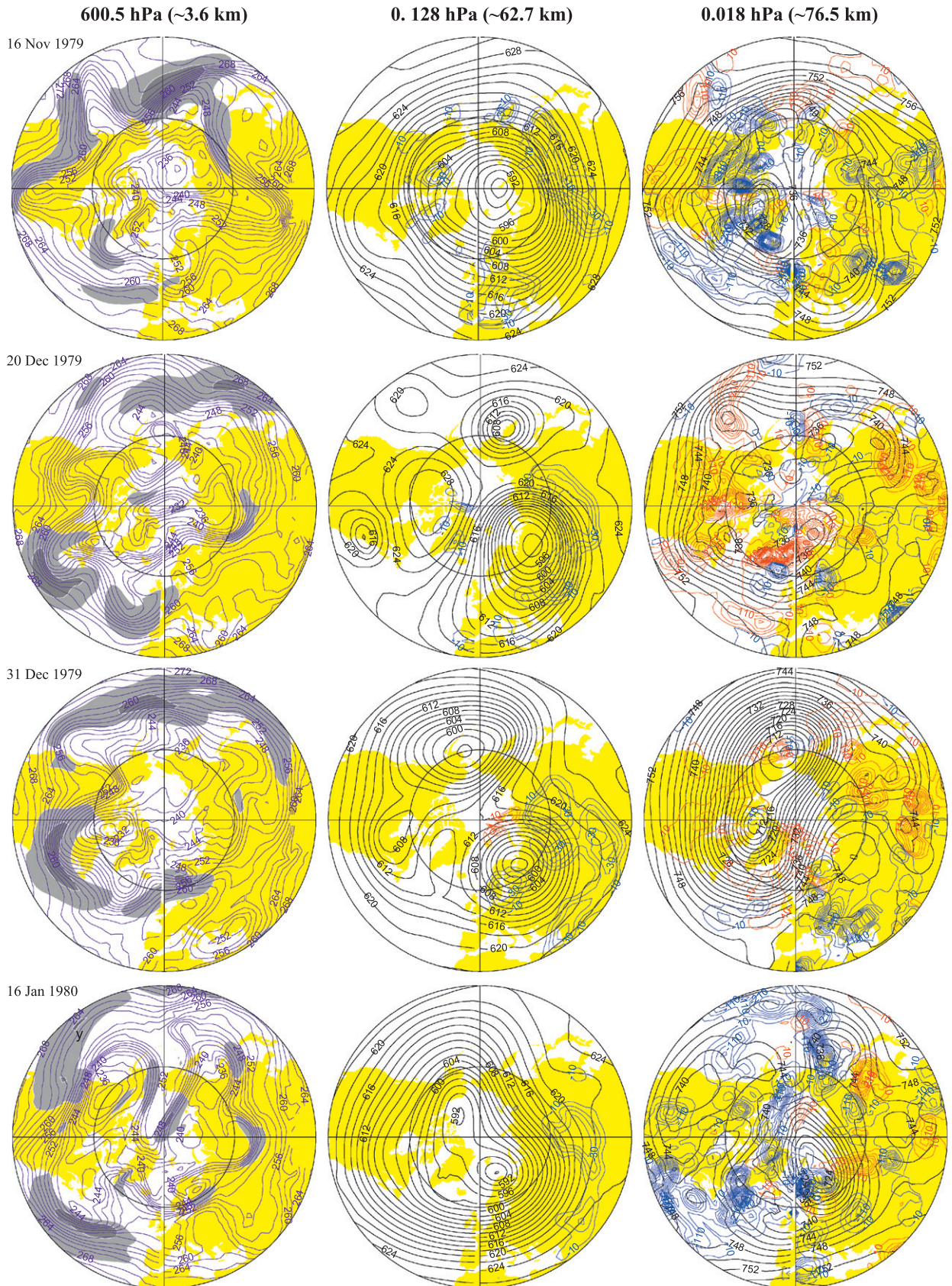
Fig. 6. Polar stereographic plots of temperature (contour) and wind speed (shaded for greater than 30, 40, 50 m s^{-1}) at ~3.6 km (left); geopotential height (black contours) and GW drag due to orography (red/blue contours; contoured every 10 m s^{-1} day^{-1} starting from 10 m s^{-1} day^{-1}) at ~62.7 km (center); and geopotential height (black contours) and GW drag due to frontogenesis (red/blue contours; contoured every 30 m s^{-1} day^{-1} starting from 10 m s^{-1} day^{-1}) at ~76.5 km (right). Red (blue) is positive (negative) values. The 60°N latitude circle is shown.

The distribution of peak orography GWD at 63 km tends to appear along the vortex's edge. Its impact in the polar region diminishes as the stratospheric wind reverses direction as noted in Fig. 3d. The appearance of orography GWD on the vortex's edge concur with mesoscale GW simulations of Limpasuvan et al. (in review) and observations of Duck et al. (2001), Wang and Alexander (2009), and Yamashita et al. (2010). However, as noted by Sato and Yoshiki (2008), GWs around the polar vortex can also be generated by local adjustment process due to unbalanced flow (also Limpasuvan et al., in review). At present, WACCM GWD parameterization does not account for these traveling waves.

4. Meridional cross-sections

For completeness, we present the meridional cross-sections of the wave forcing and circulation during key dates. As the major SSW begins on December 20, the polar night jet becomes westward over a deep layer between 40 and 70 km (Fig. 7a). This wind reversal is consistent with the large negative wind anomalies in

that altitude range and the underlying warming anomalies around 40 km associated with the fallen stratopause (Fig. 7b). Here, the anomalies are determined as the difference between the total field and its climatological value for that day computed from the 55-year WACCM run. Poleward of 40°N, positive NH wind anomalies (reddish filled contours) indicate that winds above the upper mesospheric and in the troposphere is stronger than normal while the LMUS wind is much weaker than usual (bluish filled contours). These NH wind anomalies are consistent with the temperature anomalies via thermal wind balance. For example, the polar warm (cold) anomalies centered near 40 km (70 km) would lead to anomalously weak (strong) vertical wind shear as reflected in the wind anomalies.

The anomalous NH poleward motion around 1 hPa and downward motion just below 1 hPa account for the adiabatic warming of the fallen stratopause (plots on right column). From Fig. 7a, we see that around 1 hPa the wave forcing is due to intense PW EP flux convergence near the zero wind line (as noted in the previous section). The NH polar jet above 70 km is now much stronger than usual by as much as $20-30 \text{ m s}^{-1}$, and is associated with the
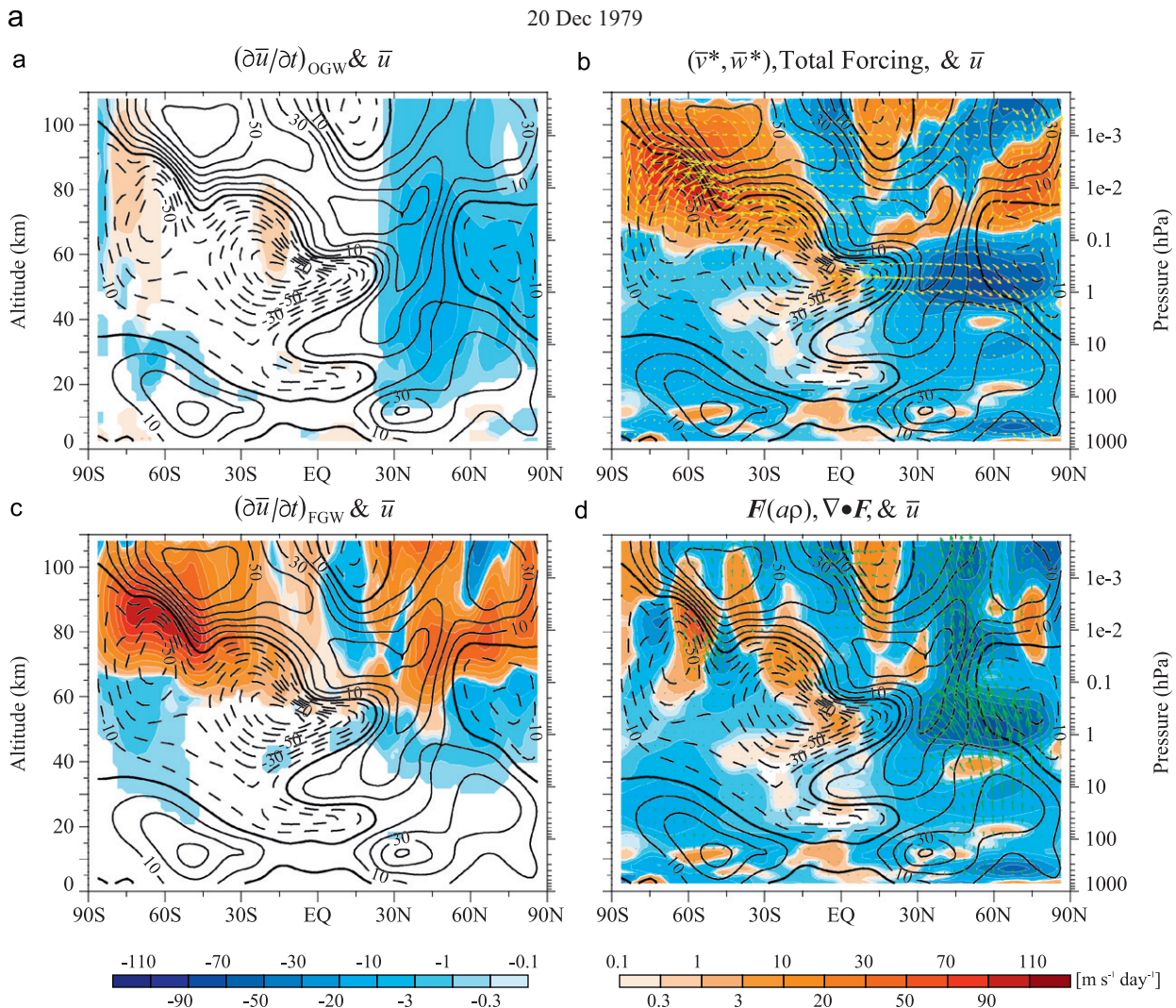

Fig. 7. (a) Meridional cross-sections of the zonal–mean zonal wind (line contour), wave forcing (filled contours). The wave forcings are the GW due to orography (a-a), the total wave forcing (a-b), GW due to frontogenesis (a-c), and resolved wave (a-d; predominantly PWs). Yellow (green) vectors represent the residual circulation (EP flux). The EP flux vectors are scaled by the product of the earth's radius and density to accentuate vectors in the middle atmosphere. (b) Meridional cross-sections of the zonal–mean zonal wind, temperature, and the meridional circulation and their anomalies (as filled contours). The total wind and temperature fields are shown as line contours while the total meridional circulation is shown as vectors. In the right column, the $\overline{v}^*(\overline{w}^*)$ anomalies are shown in the top (bottom).
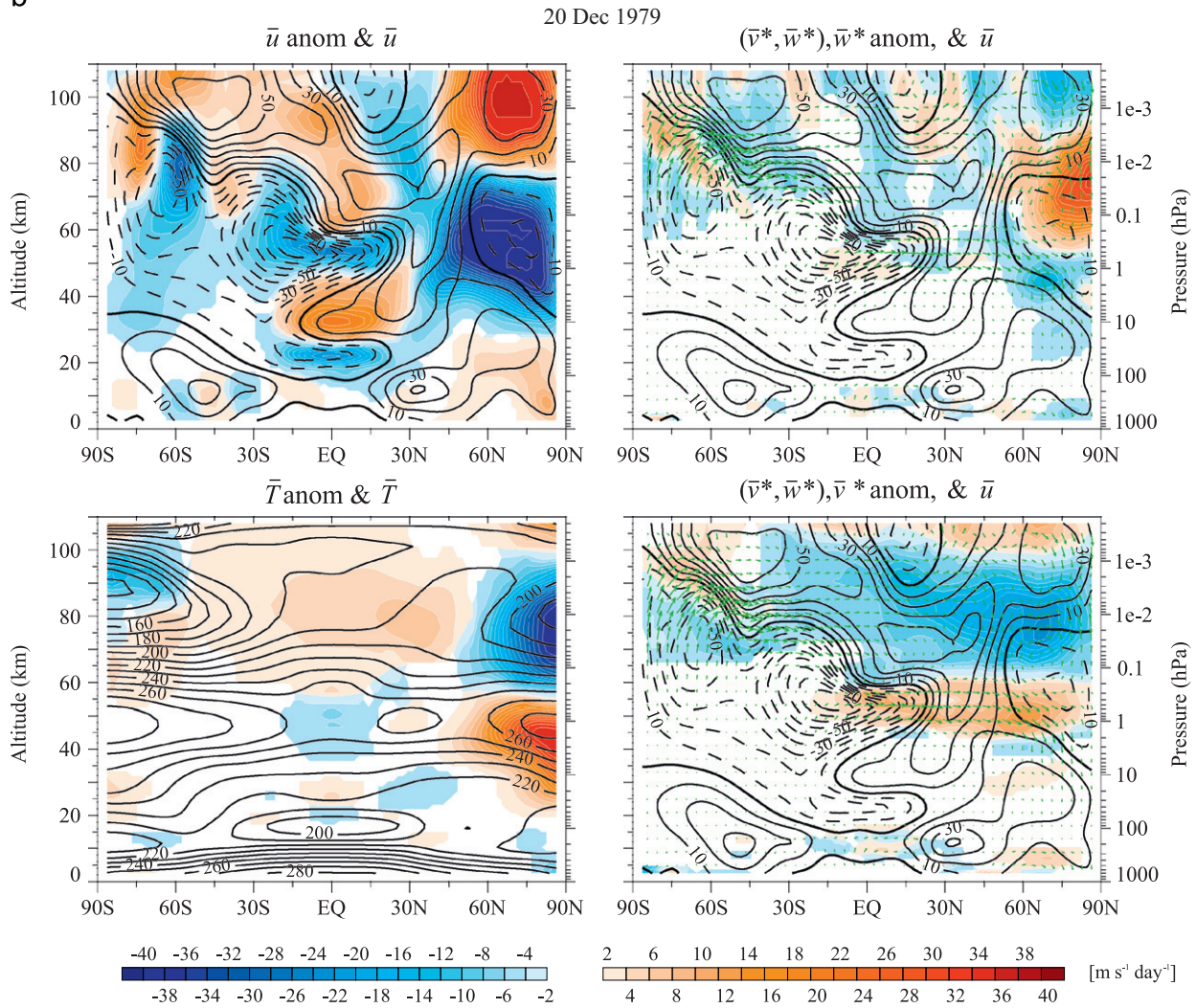
b

Fig. 7. (*Continued*)

anomalously strong cooling and upward (and equatorward) polar motion above the fallen stratopause (see Fig. 1b–d). This strong upward motion is driven mainly by the strong eastward frontogenesis GWD around 80 km and poleward of 40°N. The presence of the westward polar wind during SSW filters out much of the westward GWD forcing noted on November 16 (see top two rows and last column of Fig. 6).

As the SSW matures on December 31, the NH temperature and wind anomalies noted on December 20 persist with diminished amplitudes and a slight drop in altitude (Fig. 8a and b). Above 70 km, while frontogenesis GWD remains predominantly eastward in the NH polar region, the total wave forcing is now mainly westward and due to the strong PW flux convergence poleward of 30°N (as noted in Fig. 4a). This PW forcing drives a strong poleward and downward motion between 80 and 100 km (as seen in the residual circulation anomalies). Since this PW forcing (and the residual downward motion) tends to align with the zero wind line above the anomalous westward jet core as shown in Figs. 1d and 3b, the resulting adiabatic warming of the polar region may lead to the eventual reformation of the stratopause at an initial altitude above its climatological position as suggested by the warm anomaly around 80 km between 60°N and 90°N.

By January 16, the NH polar jet above 45 km returns to the eastward direction (Fig. 9a and b). Above 60 km, the NH frontogenesis GWD is now predominantly westward and accounts for the majority of the total wave forcing once again. This GWD forcing induces the anomalous downward and poleward over the winter pole. The alternating wind and temperature anomalies over the NH polar region noted on December 31 continue to descend toward the surface. However, a new warm anomaly is present between 70 and 80 km over the pole with the appearance of a reformed stratopause. As seen in Fig. 1, the stratopause gradually drops back toward its climatological motion after January 16.

The presence of westward wind anomaly at the surface in the high winter latitude on January 16 (Fig. 9b) projects strongly onto the anomalous wind pattern associated with the Northern Hemisphere Annular Mode (NAM; Limpasuvan and Hartmann, 1999; Thompson and Wallace, 2000). As the leading mode of wintertime climatology that describes the meridional shifting of the atmospheric mass across the Arctic Circle, the NAM phase can be biased to its negative state following the occurrence of SSW (Baldwin and Dunkerton, 1999; Limpasuvan et al., 2004). Fig. 10 shows that the NAM index (from the WACCM simulation) indeed shifts to its negative state as the upper stratospheric eastward

wind (at ∼1 hPa) returns in the winter polar region (around January 9) (Orsolini et al., 2011). Here, the NAM index is taken to be the (normalized) leading principal component of the 55-year sea level anomalies, as defined by Thompson and Wallace (2000). The negative NAM reflects a meteorological state in which the mid-latitude tropospheric jet (and synoptic disturbances) tend to be more equatorward than its climatological position.

5. Summary and discussion

In the present paper, we provide a first detailed look at the dynamics during a realistic major SSW, as simulated by the latest WACCM simulation. With parameterized GWD based largely on model-predicted quantities and the inclusion of mountain stresses that accounts for non-resolved orography, the current WACCM has very realistic NH winter climatology (Garcia et al., in preparation) with an occurrence SSW rate on par with observations (Richter et al., 2010). In the selected simulation case, the major SSW is characterized by a separation of the warm stratopause layer.

A strong interplay between GW and PW forcing is evident in the simulation as the middle atmosphere undergoes a major SSW and eventually recovers. Climatologically, westward GWD drives the polar atmosphere above the 45 km in promoting poleward and downward motion over the region throughout the winter. This

forcing helps to maintain a warm stratopause layer centered around 60 km and keeps the polar night jet weaker than it would be otherwise due strictly to radiative cooling (Hitchman et al., 1989). When the winter circumpolar wind becomes anomalously weak, EP flux due to PWs persistently converges in that weakened wind region to initiate SSW. This flux convergence provides a strong westward forcing that leads to an extensive area of wind reversal (to the westward direction) in the polar mesosphere and the upper stratosphere (e.g. around December 20). The lower boundary of the resulting westward wind pocket (marked by the zero-wind surface) then serves as focal area for further interactions between PW and the mean flow and descends in time toward the lower stratosphere. The descent is marked by the falling stratopause layer along the zero-wind surface and is maintained by the falling PW forcing that induces poleward/downward motion (and adiabatic warming over the pole). The role of PW-mean flow interaction in promoting anomalous wind descent into the lower stratosphere during SSW has been noted by Baldwin and Dunkerton (2001) and Limpasuvan et al. (2004).

Both the stratopause descent into the lower stratosphere and its reformation at high altitude has strong implications for the strato-spheric chemistry. In our companion paper, Kvissel et al. (under review) reports an intrusion of CO-rich mesospheric air into the lower stratosphere, and changes in the secondary and tertiary ozone maxima in the mesosphere.
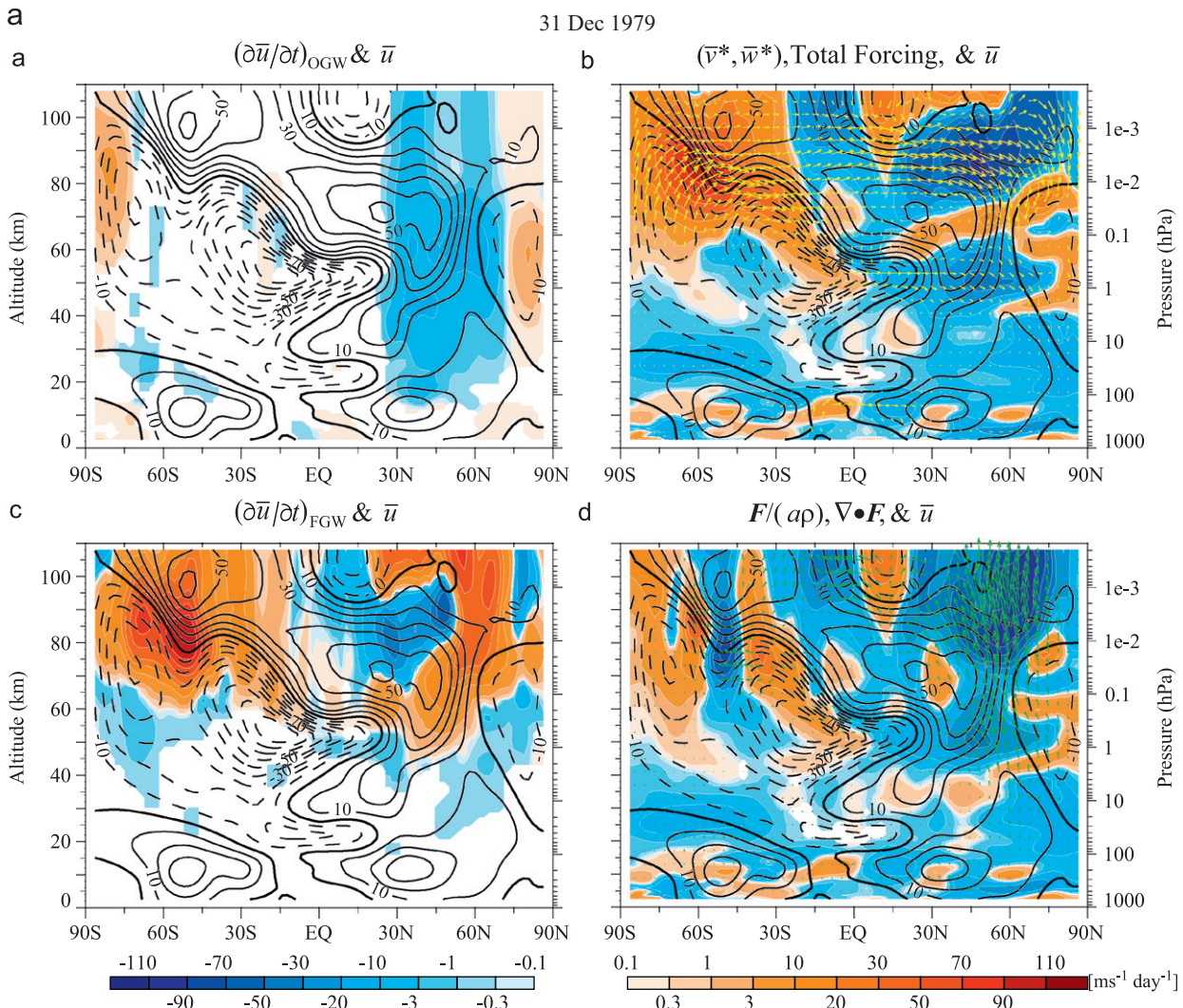

Fig. 8. (a) Same as Fig. 7a except for December 31. The vector lengths are scaled with respect to those shown in Fig. 7a. (b) Same as Fig. 7b except for December 3.
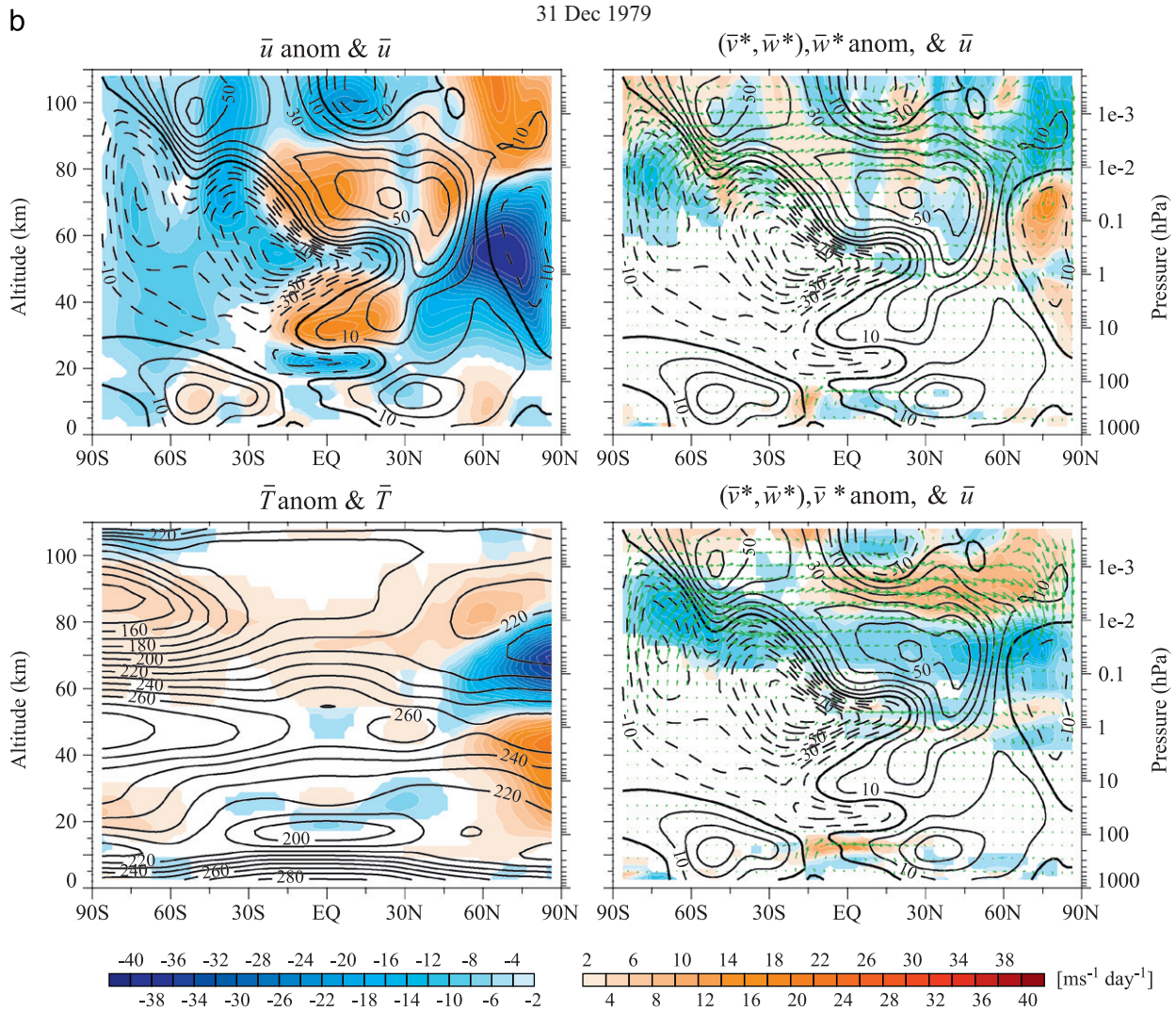
Fig. 8. (*Continued*)

The presence of the westward wind pocket over the polar region then markedly changes the wave forcing and circulation from climatology. First, the altered wind filters out much of the previously dominant westward GWD and allows eastward GWD to appear in the upper mesosphere (and lower thermosphere). The missing westward GWD (and the related circulation) then causes the stratopause to separate downward from its climatological position (Hitchman et al., 1989; Siskind et al., 2005) as noted above. The presence of the anomalous eastward GWD reverses the climatological westward wind in the upper mesosphere to the eastward direction (a change that is out of phase with anomalies below). This forcing also induces strong upward motion that cools the lower mesosphere near the region where the stratopause previously existed.

The westward wind pocket over the polar region also refracts more PW EP flux (mainly of wavenumber-1 component) into the upper mesosphere and lower thermosphere (Fig. 8a). Further investigation is needed to address the nature of this PW disturbance at these high altitudes. Smith (1996; 2003) and Liu and Roble (2002) suggested that, during SSW, the structural asymmetries imposed by GWDs can potentially force secondary PWs in the mesosphere. However, other transient PWs may also be possible. Regardless, shortly after the SSW onset, the convergence of the PW flux near the upper boundary of the westward wind pocket (marked by the zero-wind surface) results in a strong

westward forcing that promotes upper mesospheric wind recovery and induces downward motion over the pole. The continual interaction between PW and the mean flow (and the induced strong downward motion) leads to the descent of the zero-wind surface into the upper stratosphere. This pronounced downward pattern promotes a large polar warming anomaly between 75 and 80 km and the possible reformation of a stratopause at an elevated level. As the pattern descends with the zero-wind surface, the stratopause returns back toward its climatological position accompanied by the intrusion of upper mesospheric/ lower thermospheric into the upper stratospheric region (e.g. Randall et al., 2009). With the return of the warm stratopause layer, SSW concludes and westward GWD resumes its influence by driving downward circulation and keeping the night jet warmer and away from radiative equilibrium.

From time snapshots of meridional cross-sections (Figs. 7–9), we note that, while dramatic NH circulation changes are occurring as the result of SSW, changes in atmosphere south of 40°N are also present in the simulation. From December 1 to 23, plot sequence (not shown) reveals that the westward wind layer extending across the equator between 50 and 70 km penetrates further northward and becomes more vertically confined into a narrow "tongue" (as can be seen in Fig. 7). Subsequently, the wind shear around 55 km becomes very large, as evidenced by the tightening of the dashed lines.

Concurrently, strong westward PW forcing appears near the lower boundary of the westward wind region (50–60 km) in the NH polar region (e.g. Figs. 4 and 7a) as result of EP flux convergence. The induced motion by this forcing leads to anomalous poleward winds around 1 hPa that extends southward across the equator (see Fig. 7b).

Typically, the equatorial westward wind in the region near the stratopause tends to have strong vertical and meridional wind shear around the NH winter solstice. Subsequently, the jet can become barotropically/baroclinically unstable, which leads to a recurring westward propagating planetary wave disturbance called the "quasi-two-day wave" (QTDW) shortly after the solstice (Limpasuvan et al., 2000a; Orsolini et al., 1997). Indeed, QTDW is seen in the simulation in the summer easterly winds as zonal wavenumber 3 and 4 features. As such, the anomalous strong PW forcing during a major SSW (as suggested here) can lead to an equatorial westward wind with even stronger shear and, subsequently, and anomalous QTDW behavior as suggested by Limpasuvan et al. (2000b) and observed during the 2005/2006 SSW (Limpasuvan and Wu, 2009).

The dramatic NH circulation changes during the simulated major SSW are also reflected in the changes in the summer polar mesopause. Time-averaged meridional cross-sections of the zonal–mean zonal wind, temperature, and residual circulation

anomalies from December 29 to January 5 are very similar to the plots shown in Fig. 8b. The start of this time period is about two weeks after the peak upper stratospheric PW forcing (around December 16) when the stratospheric wind reversal commences (see Fig. 1). Between 50° and 90°S and around 60 to 90 km, we note moderate warm anomalies around 4–8 K in a region that is typically the coldest in the atmosphere. This warming is accompanied by weaker than normal upward/equatorward motion in the summer polar mesosphere.

Overall, these anomalies simulated in WACCM (as shown in Fig. 8b) suggest the occurrence of inter-hemispheric coupling (IHC), first proposed by Becker and Schmitz (2003) based on numerical simulations and by Karlsson et al. (2007) based on observations of inter-annual variations in mesospheric noctilucent cloud occurrences. The mechanism behind the IHC has been further analyzed by Karlsson et al. (2009a) in the Canadian Middle Atmosphere Model (CMAM) simulations and by Kornich and Becker (2010) in a mechanistic model. Furthermore, Karlsson et al. (2009b) showed its relevance on intra-seasonal time scales. These authors illustrate that, 10–15 days after an unusually strong upward PW flux at 100 hPa in the winter polar region, the typically cold summer mesopause can become at least 3 K warmer. The IHC involves a modulation and feedback of GWD in the summer hemisphere induced by zonal wind anomalies associated to anomalous cross-equatorial flow. While a
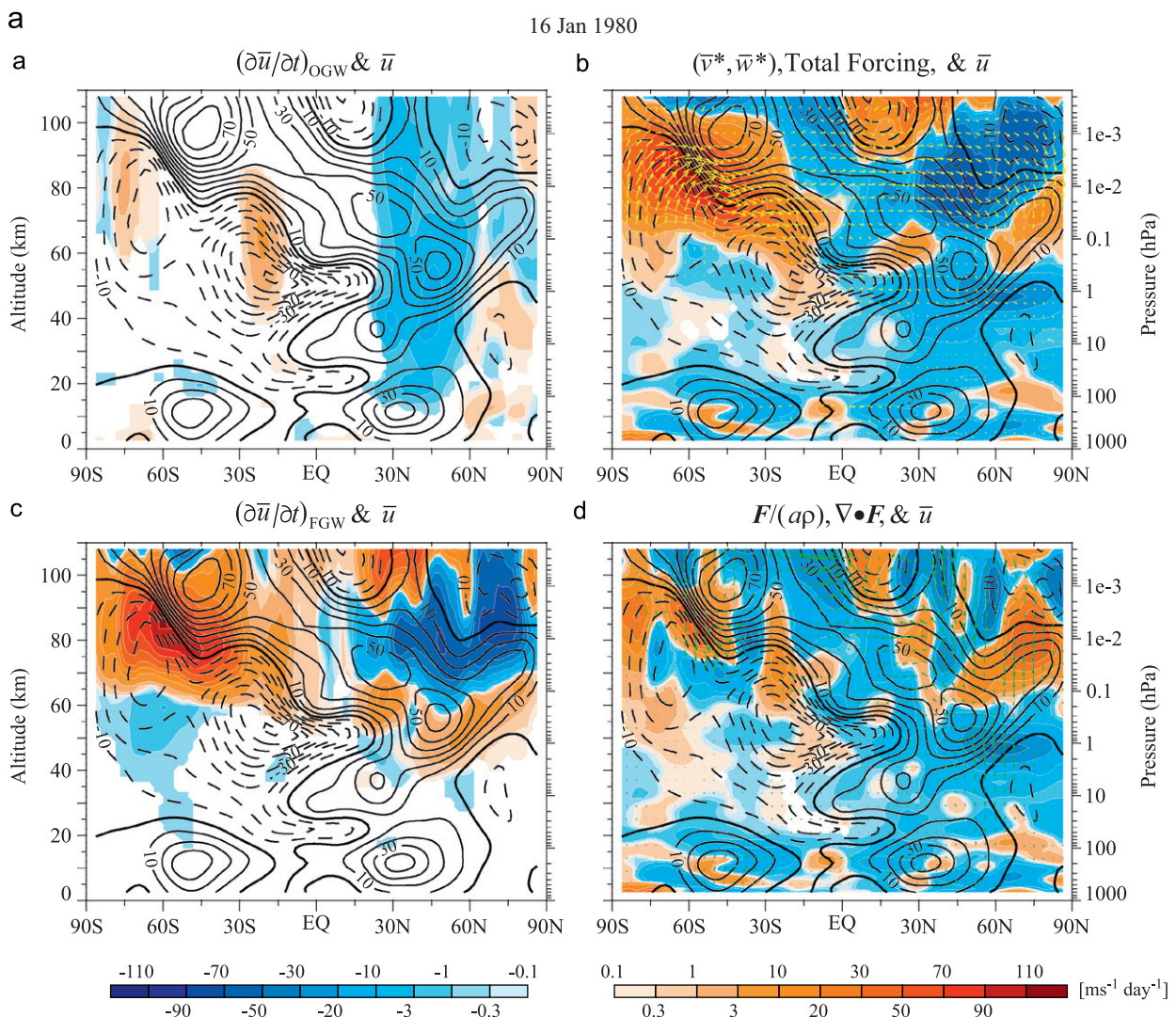

Fig. 9. (a) Same as Fig. 7a except for January 16. The vector lengths are scaled with respect to those shown in Fig. 7a. (b) Same as Fig. 7b except for January 16.
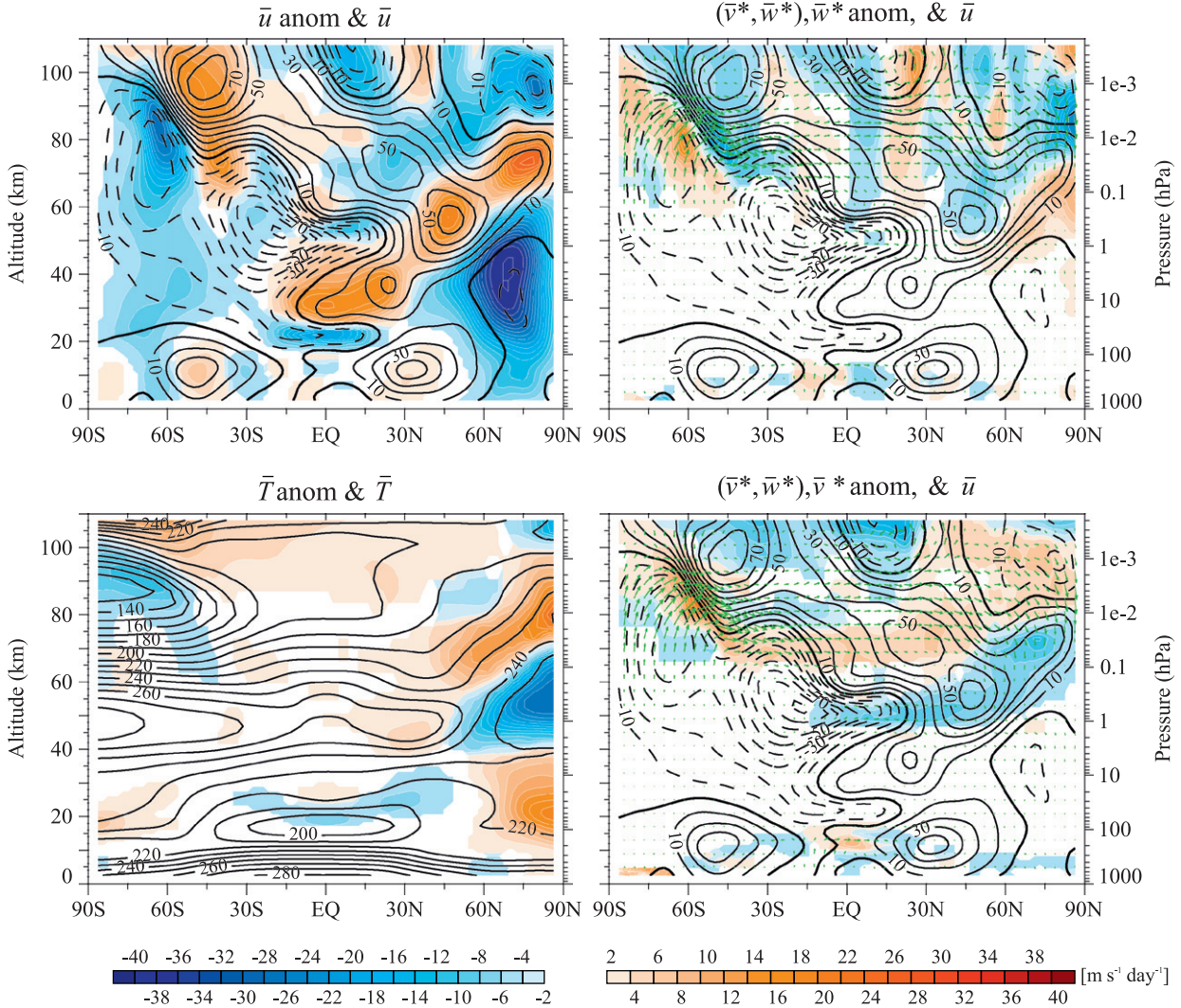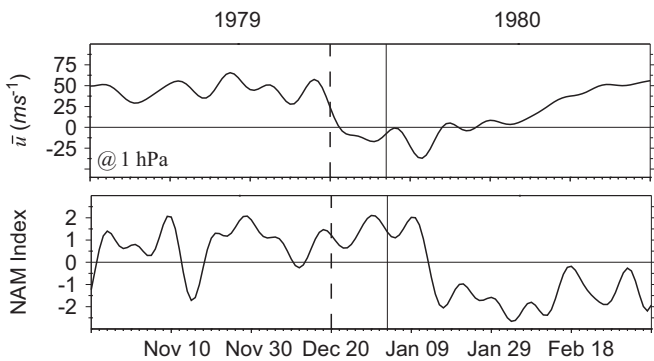
b

16 Jan 1980

Fig. 9. (Continued)

Fig. 10. Time series of the zonal–mean zonal wind at 1 hPa averaged between 60ºN–80ºN (top) and the NAM index (bottom). The (normalized) leading principal component of the 50-year WACCM sea level pressure anomalies is used as the NAM index. The solid vertical line marks January 1 and the dash line indicate the time when the zonal wind undergoes the strongest wind deceleration which then leads to wind reversal toward the westward direction. Note the shift of the NAM index to the negative phase after the wind reversal.

detailed study of this mechanism is beyond the scope of this paper, the temperature anomalies throughout the atmosphere seen here in Fig. 8b indeed bear a strong resemblance (in magnitude and position) to figure 6 of Karlsson et al. (2009a).

References

Andrews, D.G., Holton, J.R., Leovy, C.B., 1987. Middle Atmosphere Dynamics. Academic Press, 490 pp.

Baldwin, M.P., Dunkerton, T.J., 1999. Propagation of the Arctic oscillation from the stratosphere to the troposphere. J. Geophys. Res. 104, 30937–30946.

Baldwin, M.P., Dunkerton, T.J., 2001. Stratospheric harbingers of anomalous weather regimes. Science 294, 581–584.

Becker, E., Schmitz, G., 2003. Climatological effects of orography and land–sea contrasts on the gravity-wave driven circulation of the mesosphere. J. Atmos. Sci 60, 103–118.

Beres, J.H., Garcia, R.R., Boville, B.A., Sassi, F., 2005. Implementation of a gravity wave source spectrum parameterization dependent on the properties of convection in the whole atmosphere community climate model (WACCM). J. Geophys. Res. 110, D10108. doi:10.1029/2004JD005504.

Charlton, A.J., Polvani, L.M., Perlwitz, J., Sassi, F., Manzini, E., Shibata, K., Pawson, S., Nielsen, J.E., Rind, D., 2007. A new look at stratospheric sudden warming. Part ii: evaluation of numerical model simulations. J. Clim. 20, 470–488.

Duck, T.J., Whiteway, J.A., Carswell, A.I., 2001. The gravity wave–arctic stratospheric vortex interaction. J. Atmos. Sci. 58, 3581–3596.

Dunkerton, T.J., Hsu, C.-P.F., McIntyre, M.E., 1981. Some Eulerian and Lagrangian diagnostics for a model stratospheric warming. J. Atmos. Sci. 38, 819–843.

Fritts, D.C., Alexander, M.J., 2003. Gravity wave dynamics and effects in the middle atmosphere. Rev. Geophys. 41 (1), 1003. doi:10.1029/2001RG000106.

Garcia, R.R., Boville, B.A., 1994. "Downward control" of the mean meridional circulation and temperature distribution of the polar winter stratosphere. J. Atmos. Sci 51, 2238–2245.

Garcia, R.R., Marsh, D.R., Kinnison, D.E., Boville, B.A., Sassi, F., 2007. Simulation of secular trends in the middle atmosphere, 1950–2003. J. Geophys. Res. 112, D09301. doi:10.1029/2006JD007485.

Garcia, R.R., de la Torre, L., Barriopedro, D. Climatology of stratospheric sudden warming in the Whole Atmosphere Community Climate Model, in preparation.

Hitchman, M.H., Gille, J.C., Rodgers, C.D., Brasseur, G., 1989. The separated polar winter stratopause: a gravity wave driven climatological feature. J. Atmos. Sci. 46 4310–422.

Holton, J.R., 1983. The influence of gravity wave breaking on the general circulation of the middle atmosphere. J. Atmos. Sci 40, 2497–2507.

Hoskins, B.J., 1982. The mathematical theory of frontogenesis. Annu. Rev. Fluid Mech. 14, 131–151.

Hsu, C.-P.F., 1981. A numerical study of the role of wave–wave interactions during sudden stratospheric warm. J. Atmos. Sci 38, 189–214.

Karlsson, B., Kornich, H., Gumbel, J., 2007. Evidence for interhemispheric stratosphere–mesosphere coupling derived from noctilucent cloud properties. Geophys. Res. Lett. 43, L16806. doi:10.1029/2007GL030282.

Karlsson, B., McLandress, C., Shepherd, T.G., 2009a. Inter-hemispheric mesospheric coupling in a comprehensive middle atmosphere model. J. Atmos. Sol.-Terr. Phys. 71, 518–530. doi:10.1016/j.jastp.2008.08.006.

Karlsson, B., Randall, C.E., Benze, S., Mills, M., Harvey, V.L., Bailey, S.M., Russel III, J.M., 2009b. Intra-seasonal variability of polar mesospheric clouds due to Inter-hemispheric coupling. Geophys. Res. Lett. 36, L20802. doi:10.1029/2009GL040348.

Kornich, H., Becker, B., 2010. A simple model for the interhemispheric coupling of the middle atmosphere circulation. Adv. Space Res. 45, 661–668. doi:10.1016/j.asr.2009.11.001.

Kvissel, O.K., Orsolini, Y.J., Stordal, F., Limpasuvan, V., Richter, J., Marsh, D. Mesospheric intrusion and anomalous chemistry during and after a major stratospheric sudden warming characterized by an elevated stratopause in WACCM, under review.

Lee, J.N., Wu, D.L., Manney, G.L., Schwartz, M.J., Lambert, A., Livesey, N.J., Minschwaner, K.R., Pumphrey, H.C., Read, W.G., 2011. Aura microwave limb sounder observations of the polar middle atmosphere: dynamics and transport of CO and H_2O. J. Geophys. Res. 116, D05110. doi:10.1029/2010JD014608.

Limpasuvan, V., Leovy, C.B., Orsolini, Y.J., 2000a. Observed temperature two-day wave and its relatives near the stratopause. J. Atmos. Sci. 57, 1689–1701.

Limpasuvan, V., Leovy, C.B., Orsolini, Y.J., Boville, B.A., 2000b. A numerical simulation of the two-day wave near the stratopause. J. Atmos. Sci. 57, 1702–1717.

Limpasuvan, V., Hartmann, D.L., 1999. Eddies and the annular modes of climate variability. Geophys. Res. Lett. 26, 3133–3136.

Limpasuvan, V., Thompson, D.W.J., Hartmann, D.L., 2004. The life cycle of Northern Hemisphere sudden stratospheric warmings. J. Clim 17, 2584–2596.

Limpasuvan, V., Wu, D.L., 2009. Anomalous two-day wave behavior during the 2006 austral summer. Geophys. Res. Lett. 36, L04807. doi:10.1029/2008GL036387.

Limpasuvan, V., Alexander, M.J., Orsolini, Y.J., Wu, D.L., Xue, M., Richter, J.H., Yamashita, C. Mesoscale simulations of gravity waves during the 2009 major stratospheric sudden warming. J. Geophys. Res, in review.

Lindzen, R.S., 1981. Turbulence and stress owing to gravity wave and tidal breakdown. J. Geophys. Res. 86 (C10), 9707–9714.

Liu, H.-L., Roble, R.G., 2002. A study of a self-generated stratospheric sudden warming and its mesospheric-lower thermospheric impacts using the coupled TIME-GCM/CCM3. J. Geophys. Res. 107 (D23), 4695. doi:10.1029/2001JD001533.

Manney, G.L., et al., 2008a. High Arctic in extreme winters: vortex, temperature, and MLS and ACE-FTS trace gas evolution. Atmos. Chem. Phys. 8, 505–522.

Manney, G.L., et al., 2008b. The evolution of the stratopause during the 2006 major warming: data and assimilated meteorological analyses. J. Geophys. Res. 113, D11115. doi:10.1029/2007JD009097.

Manney, G.L., Schwartz, M.J., Krueger, K., Santee, M.L., Pawson, S., Lee, J.N., Daffer, W.H., Fuller, R.A., Livesey, N.J., 2009. Aura microwave limb sounder observations of dynamics and transport during the record-breaking 2009 arctic stratospheric major warming. Geophys. Res. Lett. 36. doi:10.1029/2009GL038586.

Matsuno, T., 1971. A dynamical model of the stratospheric sudden warming. J. Atmos. Sci. 28, 1479–1494.

McFarlane, N.A., 1987. The effect of orographically excited wave drag on the general circulation of the lower stratospheric and troposphere. J. Atmos. Sci 44, 1775–1800.

McLandress, C., Scinocca, J.F., 2005. The GCM response to current parameterizations of nonorographic gravity wave drag. J. Atmos. Sci. 62, 2394–2413.

Orsolini, Y.J., Limpasuvan, V., Leovy, C.B., 1997. The tropical stratopause in the UKMO stratospheric analyses: evidence for a 2-day wave and inertial circulations. Q. J. R. Met. Soc. 123, 1707–1724.

Orsolini, Y.J., Urban, J., Murtagh, D.P., Lossow, S., Limpasuvan, V., 2010. Descent from the polar mesosphere and anomalously high stratopause observed in 8 years of water vapor and temperature satellite observations by the odin sub-millimeter radiometer. J. Geophys. Res. 115, D12305. doi:10.1029/2009JD013501.

Orsolini, Y.J., Kindem, I.T., Kvamsto, N.G., 2011. On the potential impact of the stratosphere upon seasonal dynamical hindcasts of the North Atlantic oscillation: a pilot study. Clim. Dyn. 36. doi:10.1007/s00382-009-0705-6 2011.

Pawson, S., 1997. Effects of gravity wave drag in the Berlin troposphere–stratosphere–mesosphere GCM. In: Hamilton, K. (Ed.), Gravity Wave Processes: Their Parametrization in Global Climate Models, NATO ASI Series, Series I, vol. 50. Springer, New York, pp. 327–336.

Randall, C.E., et al., 2009. NO_x descent in the Arctic middle atmosphere in early 2009. Geophys. Res. Lett., L18811. doi:10.1029/2009GL039706.

Ren, S., Polavarapu, S.M., Shepherd, T.G., 2008. Vertical propagation of information in a middle atmosphere data assimilation system by gravity–wave drag feedbacks. Geophys. Res. Lett. 35, L06804. doi:10.1029/2007GL032699.

Richter, J.H., Sassi, F., Garcia, R.R., 2010. Towards a physically based gravity wave source parameterization. J. Atmos. Sci. 67. doi:10.1175/2009JAS3113.1.

Sato, K., Kumakura, T., Takahashi, M., 1999. Gravity waves appearing in a high-resolution GCM simulation. J. Atmos. Sci. 56, 1005–1018.

Sato, K., Yoshiki, M., 2008. Gravity wave generation around the polar vortex in the stratosphere revealed by 3-hourly radiosondes observations at Syowa station. J. Atmos. Sci, 3719–3735. doi:10.1175/2009JAS2539.1.

Siskind, D.E., Coy, L., Espy, P., 2005. Observations of stratospheric warmings and mesospheric coolings by the TIMED SABER instrument. Geophys. Res. Lett. 32, L09804. doi:10.1029/2005GL022399.

Smith, A.K., 1996. Longitudinal variations in mesospheric winds: evidence for gravity wave filtering by planetary waves. J. Atmos. Sci. 53, 1156–1173.

Smith, A.K., 2003. The origin of stationary planetary waves in the upper mesosphere. J. Atmos. Sci. 60, 3033–3041.

Thayer, J.P., Livingston, J.M., 2008. Observations of wintertime arctic mesosphere cooling associated with stratosphere baroclinic zones. Geophys. Res. Lett. 35, L18803. doi:10.1029/2008GL034955.

Thompson, D.W.J., Wallace, J.M., 2000. Annular modes in the extratropical circulation. Part I: month-to-month variability. J. Clim. 13, 1000–1016.

von Zahn, U., Fiedler, J., Naujokat, B., Langematz, U., Krüger, K., 1998. A note on recordhigh temperatures at the northern polar stratopause in winter 1997/98. Geophys. Res. Lett. 25 (22), 4169–4172. doi:10.1029/1998GL900091.

Watanabe, S., Kawatani, Y., Tomikawa, Y., Miyazaki, K., Takahashi, M., Sato, K., 2008. General aspects of a T213L256 middle atmosphere general circulation model. J. Geophys. Res. 113, D12110. doi:10.1029/2008JD010026.

Wang, L., Alexander, M.J., 2009. Gravity wave activity during stratospheric sudden warmings in the 2007–2008 Northern Hemisphere winter. J. Geophys. Res. 114, D18108. doi:10.1029/2009JD011867.

Yamashita, C., Liu, H.-L., Chu, X., 2010. Gravity wave variations during the 2009 stratospheric sudden warming as revealed by ECMWF-T799 and observations. Geophys. Res. Lett. 37, L22806 doi:10.1029/2010GL045437.

Zhang, G.J., McFarlane, N.A., 1995. Role of convection scale momentum transport in climate simulation. J. Geophys. Res. 100 (D1), 1417–1426.